Nanoscale Advances

PAPER

View Article Online
View Journal | View Issue

Cite this: *Nanoscale Adv.*, 2019, **1**, 154

Rational design of C_2N-based type-II heterojunctions for overall photocatalytic water splitting†

Xu Zhang, An Chen, Zihe Zhang, Menggai Jiao and Zhen Zhou *

Photocatalytic water splitting is a promising method for the production of clean energy and searching for efficient photocatalysts has received extensive attention. Fabricating type-II heterojunctions is an effective approach to improve the photocatalytic efficiency. Based on the band edge positions and lattice parameters, we found that several kinds of monochalcogenide monolayers can be used to fabricate type-II heterojunctions with C_2N monolayers. C_2N/GaTe and C_2N/InTe van der Waals (vdW) heterojunctions were investigated as potential photocatalysts for water splitting by means of first-principles computations. Both are type-II heterojunctions, and could promote the efficient spatial separation of electron–hole pairs. Their band edges straddle water redox potentials, satisfying the requirements for photocatalytic water splitting. Besides, the high carrier mobility of C_2N/GaTe and C_2N/InTe heterojunctions implies that the transfer of carriers to reactive sites is easy, and the recombination probability of photo-generated carriers is reduced. The Gibbs free energy calculations indicate that C_2N/GaTe and C_2N/InTe heterojunctions, especially C_2N/InTe, exhibit high catalytic performance towards hydrogen and oxygen evolution reactions. Particularly, C_2N/InTe exhibits a direct band gap with strong absorption in both visible and near ultraviolet regions, indicating that it is a very promising candidate for photocatalytic water splitting. This work would provide a new idea for the development of type-II heterojunctions for photocatalytic water splitting.

Received 12th July 2018
Accepted 10th September 2018

DOI: 10.1039/c8na00084k

rsc.li/nanoscale-advances

Introduction

Photocatalytic water splitting is a promising technology to produce hydrogen with sunlight, providing a sustainable solution to address environmental and energy related issues.[1,2] The first significant breakthrough in photocatalytic overall water splitting without electric power was achieved by Fujishima and Honda.[3] Since then, many photocatalysts have been developed.[4–10] However, industrial hydrogen is primarily produced from fossil fuels since the current photocatalytic systems are not efficient and economical enough for industrial hydrogen production.[4] A low quantum yield, inability to utilize visible light and poor catalytic activity are critical obstacles for the commercial application of photocatalytic water splitting.[11,12] Therefore, the discovery of novel photohydrolytic catalysts with high efficiency plays a critical role in the development of photocatalytic water splitting.

Nanoscale materials with adjustable dimensions and shapes are one of the most promising photohydrolytic catalysts. Among various kinds of nanoscale materials, two-dimensional (2D) materials possess two main inherent advantages which can be used to improve the photocatalytic efficiency for water splitting.[11,13–15] First, 2D materials have a high surface to volume ratio, exhibiting a large specific surface area available for photocatalytic reactions and promoting the adsorption of reactants. Besides, the distance that photo-generated electrons and holes have to migrate in 2D materials is short, reducing the possibility of electron–hole recombination, thereby potentially enhancing photocatalytic activity. With the rapid development of high-performance computations, various 2D materials were designed and predicted to be promising photocatalysts for overall water splitting.[11,12,15,16] The computations have promoted the development of photocatalysts and some 2D materials have been proved to be good photocatalysts for water splitting in experiments, such as g-C_3N_4 (ref. 17) and MPS_3 (M = Fe or Mn).[18,19]

Besides, fabricating van der Waals (vdW) heterojunctions is an effective method to further improve the photocatalytic performance.[20,21] Especially, in type-II heterojunctions, both the conduction band minimum (CBM) and valence band maximum (VBM) of one layer are lower than that of the other layer. Therefore, the lowest energy states of electrons and holes are on

School of Materials Science and Engineering, National Institute for Advanced Materials, Institute of New Energy Material Chemistry, Computational Centre for Molecular Science, Nankai University, Tianjin 300350, P. R. China. E-mail: zhouzhen@nankai.edu.cn; Fax: +86 22 23498941; Tel: +86 22 23503623

† Electronic supplementary information (ESI) available. See DOI: 10.1039/c8na00084k

different layers, ensuring the effective separation of photogenerated electrons and holes. In our previous reports, we proposed a high-throughput computational material design framework to search for 2D photocatalysts and rationally design type-II heterojunctions for water splitting based on the Materials Project Database.[15] Various kinds of type-II heterojunctions were successfully designed. However, due to the rapid development of 2D materials, several novel kinds of materials, which have not been included in materials databases, have been successfully prepared in experiments. Therefore, predicting type-II heterojunctions containing novel kinds of 2D materials is necessary to evaluate their photocatalytic activity.

Recently, a novel kind of 2D material, named C_2N, has been successfully prepared by simple wet chemical reactions.[22] By means of first-principles computations, C_2N monolayers were predicted to be a promising photocatalyst for water splitting.[23] In experiments, vdW heterojunctions composed of C_2N and aza-conjugated microporous polymers were prepared, which exhibit good photocatalytic performance for overall water splitting.[24] Enlightened by the computational and experimental results, we screened the 2D monolayer materials in our previous work[15] to explore the materials which could be used to fabricate type-II heterojunctions with C_2N monolayers to further improve their photocatalytic performance. The screening criteria are consistent with our previous report.[15] First, the CBM and VBM of the layer should be lower or higher than that of C_2N, respectively. Then the lattice parameters of the layer should be close to those of C_2N (lattice mismatch <10%), which could reduce the strain, improving the stability. This could also be achieved by constructing supercells. Considering the computational cost, small supercells, such as $2 \times 2 \times 1$ supercells, were considered. Our results indicate that transition metal monochalcogenides and dichalcogenides could be used to fabricate type-II vdW heterojunctions with C_2N. Recently, C_2N/WS_2 vdW type-II heterojunctions were proposed as promising photocatalysts for water splitting.[25]

Therefore, in this work, we focused on monochalcogenide/C_2N heterojunctions. Based on the calculated band structures,[26] besides GaTe which was proposed in our previous report,[15] some other monochalcogenides, including GaSe and InTe, were also investigated. By means of first-principles computations, we designed GaSe/C_2N, GaTe/C_2N and InTe/C_2N vdW heterojunctions and investigated their stability, electronic, optical properties, carrier mobility and catalytic performance towards the hydrogen evolution reaction (HER) and oxygen evolution reaction (OER). The results indicate that GaTe/C_2N and InTe/C_2N are type-II heterojunctions, implying the efficient separation of holes and electrons, thereby preventing their recombination. The exciton binding energies of GaTe/C_2N and InTe/C_2N type-II heterojunctions are lower than that of C_2N, indicating better separation of the bound holes and electrons to free charge carriers. Both GaTe/C_2N and InTe/C_2N exhibit high carrier mobility, indicating high photocatalytic activity. Besides, InTe/C_2N exhibits an excellent catalytic performance towards the HER and OER, further proving InTe/C_2N type-II heterojunctions to be a promising candidate for overall photocatalytic water splitting.

Computational methods

First-principles computations on the basis of density functional theory (DFT) were performed by using a plane-wave basis set as implemented in the Vienna ab initio simulation package (VASP).[27] Ion-electron interactions were described with the projector augmented wave (PAW) method[28] and an energy cutoff of 550 eV was adopted for the plane-wave basis set. The generalized gradient approximation (GGA) involving the Perdew, Burke, and Ernzerhof (PBE) functional was selected to describe the exchange correlation energy.[29] The effect of the vdW interactions was dealt with the DFT-D3 method with Becke–Jonson damping.[30,31] A Monkhorst–Pack k-point mesh[32] of $5 \times 5 \times 1$ was employed for C_2N and heterojunctions and $10 \times 10 \times 1$ for monochalcogenide (MX, M = Ga, In, X = Se, Te) monolayers. In order to prevent the artificial interactions between periodic images, a vacuum space with at least 20 Å was inserted between the periodic images along the z-direction. Since the GGA functional systematically underestimates the band gaps,[33] we used the Heyd–Scuseria–Ernzerhof (HSE06) functional[34] to accurately compute the band structures and band edge positions.

The binding energy of vdW heterojunctions was calculated based on:

$$E_{\text{binding}} = E_{\text{heterojunction}} - E_{C_2N} - E_{MX}$$

where $E_{\text{heterojunction}}$, E_{C_2N} and E_{MX} represent the total energies of the heterojunctions, C_2N and monochalcogenides (GaSe, GaTe and InTe), respectively.

For inorganic semiconductors, the phonon scattering dominates the intrinsic mobility which could be described by deformation potential (DP) theory.[35] DP theory has been successfully used in predicting the carrier mobility of 2D semiconductors, including graphene,[36] phosphorene,[37] MoS_2,[38] MXenes[39] and so on.[16,40] Therefore, the carrier mobility (μ_{2D}) of isolated C_2N, GaTe, and InTe monolayers and heterojunctions could be predicted by using the phonon limited scattered mode on the basis of effective mass approximation with DP theory according to:

$$\mu_{2D} = \frac{2e\hbar^3 C}{3k_B T|m^*|^2 {E_1}^2}$$

in which $\hbar$ is the reduced Planck constant, e is the electron charge, T is the temperature and set to be 300 K, and C represents the in-plane stiffness and is given by $C = (\partial^2 E_{\text{total}}/\partial\varepsilon^2)/S_0$, where E_{total}, ε and S_0 represent the total energy of a cell, the uniaxial strain and the area of an optimized cell. m^* is the effective mass and calculated by using $m^* = \hbar^2(\partial^2 E(k)/\partial k^2)^{-1}$, in which k is the wave vector and $E(k)$ means the energy at the corresponding wave vector k. E_1 is the DP constant calculated by using $E_1 = \partial E_{\text{edge}}/\partial\varepsilon$, where E_{edge} is the energy of the CBM and VBM along the transport direction. Considering the time consumption, the carrier mobility was calculated with the PBE functional.

To investigate the optical absorption, the imaginary part of the dielectric function ε_2 was calculated based on the following equation:[41]

$$\varepsilon^2_{\alpha\beta}(\omega) = \frac{4\pi^2 e^2}{\Omega}\lim_{q\to 0}\frac{1}{q^2}\sum_{c,v,\vec{k}} 2w_{\vec{k}}\delta\left(\varepsilon_{c\vec{k}} - \varepsilon_{v\vec{k}} - \omega\right) \times \left\langle u_{c\vec{k}+e_\alpha\vec{q}}\middle|u_{v\vec{k}}\right\rangle\left\langle u_{c\vec{k}+e_\beta\vec{q}}\middle|u_{v\vec{k}}\right\rangle^*$$

where c and v refer to the conduction and valence band states, respectively, and both were determined by using the HSE06 functional here. $u_{c\vec{k}}$ represents the cell periodic part of the orbital at the k-point $\vec{k}$. The real part is obtained by using the Kramers–Kronig relationship:[42]

$$\varepsilon^1_{\alpha\beta}(\omega) = 1 + \frac{2}{\pi}P\int_0^\infty \frac{\varepsilon^2_{\alpha\beta}(\omega')\omega'}{\omega'^2 - \omega^2 + i\eta}d\omega'$$

where P indicates the principal value. The absorption coefficient $\alpha(\omega)$ was computed by using[43]

$$\alpha(\omega) = \sqrt{2}\omega\left(\sqrt{\varepsilon_1{}^2(\omega) + \varepsilon_2{}^2(\omega)} - \varepsilon_1(\omega)\right)^{1/2}$$

where ε_1 is the real part of the dielectric function, obtained from ε_2 by using the Kramer–Kronig relationship.

The HER catalytic performance of the heterojunctions was evaluated by calculating the Gibbs free energy change of the adsorption of atomic hydrogen (ΔG_H):

$$H^+ + e^- + * \xrightarrow{\Delta G_H} H*$$

in which * represents the active sites and H* represents the adsorbed intermediates. According to the computational hydrogen electrode model,[44] the chemical potential of the H^+/e^- pair under the standard conditions of pH = 0 is equal to half that of H_2 at a potential of 0 V. Here, ΔG_H can be calculated by using

$$\Delta G_H = \Delta E_H + \Delta E_{ZPE} - T\Delta S_H$$

ΔE_H represents the adsorption energy of one hydrogen atom and can be calculated based on: $\Delta E_H = E_{nH} - E_{(n-1)H} - 1/2E_{H_2}$, where E_{nH} and $E_{(n-1)H}$ stand for the total energy of the heterojunction with n and $n-1$ hydrogen atoms adsorbed, respectively, and E_{H_2} represents the total energy of gas phase H_2 calculated by DFT. ΔE_{ZPE} means the difference of the zero-point energy between the n-th adsorbed hydrogen and half of the gas phase hydrogen. ΔS_H is the entropy change between the adsorbed state and gas phase. The entropy of the adsorbed state was calculated by using[45]

$$S(T) = \sum_{i=1}^{3N}\left[-R\ln\left(1 - e^{-\frac{h\nu_i}{k_B T}}\right) + \frac{N_A h\nu_i}{T}\frac{e^{-h\nu_i/k_B T}}{1 - e^{-h\nu_i/k_B T}}\right]$$

where R is the universal gas constant, h is Planck's constant, ν_i is the normal mode frequency, N_A is Avogadro's number and N represents the number of the adsorbed atoms. The ΔG_H of a good catalyst for the HER should be close to zero.

Under acidic conditions, the mechanism for the OER process is:

$$H_2O(l) + * \xrightarrow{\Delta G_1} *OH + H^+ + e^-$$

$$*OH \xrightarrow{\Delta G_2} *O + H^+ + e^-$$

$$*O + H_2O(l) \xrightarrow{\Delta G_3} *OOH + H^+ + e^-$$

$$*OOH \xrightarrow{\Delta G_4} * + O_2(g) + H^+ + e^-$$

where (l) represents the liquid phase and (g) refers to the gas phase. To estimate the OER activity, the free energy change (ΔG) of the OER elementary steps should be calculated by:

$$\Delta G = \Delta E + \Delta E_{ZPE} - T\Delta S + \Delta G_U + \Delta G_{pH}$$

where ΔE means the reaction energy which could be obtained by DFT computations. $\Delta G_U = -eU$ and U is the electrode potential. ΔG_{pH} denotes the correction of the H^+ free energy by the concentration dependence of the entropy and is given by: $\Delta G_{pH} = k_B T\ln 10 \times pH$. Because of the inaccuracy of DFT in estimating the binding energy of O_2, the free energy of O_2 was calculated according to the free energy change of $O_2 + 2H_2 \rightarrow 2H_2O$, which is -4.92 eV.

In order to evaluate the efficiency of the separation of photogenerated charge carriers, the exciton binding energies (E_b) were calculated based on the Mott–Wannier hydrogenic model. In a previous report, the exciton binding energies of C_2N containing vdW heterojunctions were calculated based on:[25]

$$E_b = \frac{13.6\mu_{ex}}{m_e\varepsilon^2}$$

$$\mu_{ex} = \frac{m_e m_h}{m_e + m_h}$$

where μ_{ex} is the effective exciton mass and ε is the macroscopic static dielectric constant which is the sum of the ionic ε_{ion} and electronic ε_{el} contributions.

Results and discussion

Geometric structure and electronic properties of isolated monolayers

First the geometric structures of isolated monolayers were optimized and are shown in Fig. S1.† The lattice parameters are listed in Table S1,† which are consistent with reported values.[26,46]

Then the electronic properties of these monolayers were investigated at the HSE06 level as shown in Fig. S2.† The C_2N monolayer exhibits a direct band gap of 2.49 eV at the Γ point of the Brillouin zone, which agrees well with those in previous reports.[23,46] The MX monolayers (GaSe, GaTe and InTe) exhibit indirect band gaps of 2.97, 2.21 and 2.21 eV, respectively. For GaSe and InTe monolayers, the CBM is at the Γ point while the VBM is located between the Γ and K points. For the GaTe monolayer, the CBM is located at the M point. These computational results are consistent with those in the previous report,[26] indicating the reliability of our results.

Geometric structure and stability of heterojunctions

In order to match the lattice and reduce the strain, the C_2N/MX heterojunctions were constructed based on the unit cell of C_2N and 2 × 2 × 1 supercells of MX monolayers. Three high symmetry stacking patterns (Fig. S3†) were considered in this work. For pattern a, all the MX atoms are on the top of the hollow sites of the C_2N monolayers. For patterns b and c, several MX atoms are located on the top of C_2N atoms. The relative binding energies are shown in Table S2.† For all the heterojunctions, pattern a is the most stable structure and was used in the following computations.

The geometric structures, lattice parameters and binding energies of the most stable structure for the three heterojunctions are summarized in Fig. 1 and Table S3.† The distance between the C_2N and MX monolayers in these heterojunctions is about 3.40 Å (Table S3†), implying that the vdW effect plays the primary role in the interlayer interaction. Due to the large lattice mismatch for C_2N/GaSe (Table S3†), the binding energy is positive, indicating that it is unstable. For C_2N/GaTe and C_2N/InTe, their lattice mismatch is lower than 3%, ensuring the experimental feasibility. Besides, the binding energies of C_2N/GaTe and C_2N/InTe are −10.8 and −9.6 meV Å^{-2}, respectively, which are comparable to those of some typical vdW crystals, including MoS_2 (−26.0 meV Å^{-2})[47] and graphene (−12.0 meV Å^{-2}),[48] and some vdW heterojunctions, such as GaSe/graphene (−18.4 meV Å^{-2})[49] and C_3N_4/MoS_2 (−17.8 meV Å^{-2}).[50] These results further indicate that C_2N/GaTe and C_2N/InTe are stable. C_2N/GaTe and C_2N/InTe heterojunctions were investigated in the following computations.

Electronic and optical properties of heterojunctions

The electronic properties are extremely important for photocatalysts. The band structures of C_2N/GaTe and C_2N/InTe heterojunctions were calculated with the HSE06 functional as shown in Fig. 2.

The band gaps of C_2N/GaTe and C_2N/InTe heterojunctions are 1.43 and 1.52 eV, respectively, which are lower than those of isolated monolayers. The CBM of C_2N/GaTe and C_2N/InTe heterojunctions both are located at the Γ point. The VBM of C_2N/GaTe is located between the Γ and K points while the VBM of C_2N/InTe is at the Γ point. Therefore, C_2N/InTe transfers to a direct band gap semiconductor while C_2N/GaTe still possesses an indirect band gap. As shown in Fig. 2, the CBM of the heterojunctions is mainly contributed by C_2N while the VBM mostly comes from the MX. Therefore, both C_2N/GaTe and C_2N/InTe possess a typical type-II band alignment, which promotes the efficient spatial separation of electron–hole pairs, overcoming the electron–hole recombination issue. The conduction band offset (CBO) and valence band offset (VBO) were calculated to be 0.65 and 1.00 eV for C_2N/GaTe and 0.79 and 0.92 eV for C_2N/InTe. The photogenerated electrons in the CBM of GaTe or InTe could transfer to the CBM of C_2N by the chemical potential difference of CBO while the photogenerated holes in the VBM of C_2N can migrate to the VBM of GaTe or InTe *via* the chemical potential difference of VBO. The results further ensure the effective spatial separation of electron–hole pairs.

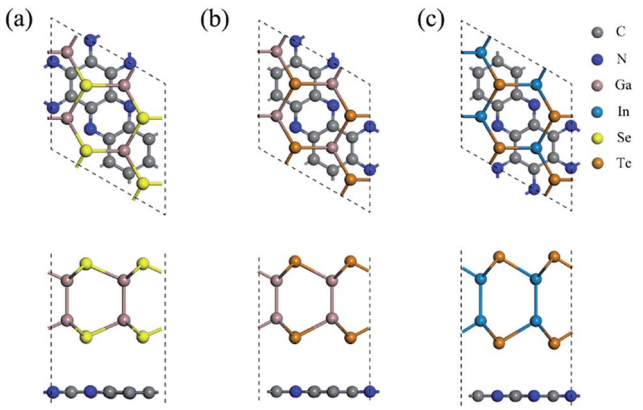

Fig. 1 Top and side views of (a) C_2N/GaSe, (b) C_2N/GaTe and (c) C_2N/InTe heterojunctions.

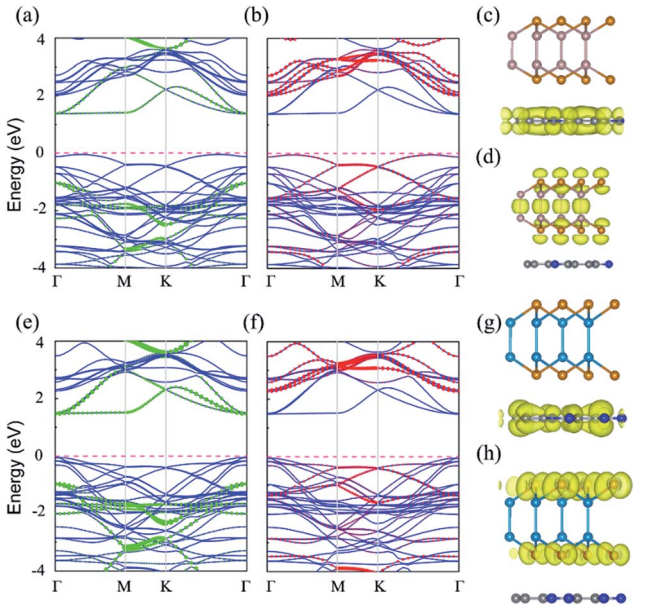

Fig. 2 Band structures of the C_2N/GaTe heterojunction projected to (a) C_2N and (b) GaTe, respectively computed with the HSE06 functional. Band structures of the C_2N/InTe heterojunction projected to (e) C_2N and (f) InTe, respectively. The sizes of green and red dots represent the weight of C_2N and GaTe (InTe). Spatial structures of wave functions for the C_2N/GaTe heterojunction at the (c) CBM and (d) VBM with an isosurface of 0.002 e Å^{-3}. Spatial structures of wave functions for the C_2N/InTe heterojunction at the (g) CBM and (h) VBM with an isosurface of 0.002 e Å^{-3}.

Besides, the partial density of states (PDOS) was also calculated to gain deep insight into the composition of the VBM and CBM of the heterojunctions as shown in Fig. S4.† The CBM mainly originates from the p states of C and N atoms while the VBM is contributed by the p states of Te and Ga (or In) atoms.

A fundamental requirement for photocatalysts for overall water splitting is that the band edges should straddle the water redox potentials. That is to say, the VBM must be lower than the oxidation potential of O_2/H_2O and the CBM should be higher than the reduction potential of H^+/H_2. Besides, the

water redox potential is influenced by the pH value.[12,15] Here, the reduction potential of H^+/H_2 is calculated by using: $E^{red}_{H^+/H_2}(vs.\ vacuum) = -4.44\ eV + pH \times 0.059\ eV$ and the oxidation potential of O_2/H_2O is $E^{ox}_{O_2/H_2O}(vs.\ vacuum) = -5.67\ eV + pH \times 0.059\ eV$. The schematic diagram for the band edge positions relative to the vacuum level of the isolated monolayers and heterojunctions is shown in Fig. 3. The band edges of all the isolated monolayers (C_2N, GaSe, GaTe and InTe) and C_2N/InTe heterojunction straddle the redox potentials of water at pH = 0. However, the VBM of the C_2N/GaTe heterojunction is higher than the oxidation potential of O_2/H_2O at pH = 0. An appropriate pH value of 1.60–4.98 is needed for the C_2N/GaTe heterojunction for photocatalytic water splitting. The results suggest that the constructed C_2N/GaTe and C_2N/InTe heterojunctions are promising candidates for photocatalytic water splitting without an external bias voltage at appropriate pH. Interestingly, the C_2N/InTe heterojunction exhibits a direct band gap.

Compared with the isolated monolayers, the band edge positions of the CBM and VBM in the heterojunctions are located closer to the redox potentials of water, suggesting higher photocatalytic efficiency and optical absorption.[51] In order to investigate the optical absorption, the average absorption coefficients of x, y and z directions were calculated as shown in Fig. 4. Besides, the imaginary parts of the dielectric function are also shown in Fig. S5.† As shown in Fig. 4 and S5,† the C_2N monolayer possesses absorption peaks in the visible spectrum while GaTe and InTe monolayers exhibit broad absorption in the near ultraviolet region. Fascinatingly, C_2N/GaTe and C_2N/InTe heterojunctions exhibit strong absorption in both visible and near ultraviolet regions with an intensity of $10^5\ cm^{-1}$. Therefore, both the C_2N/GaTe and C_2N/InTe heterojunctions are efficient light harvesting photocatalysts.

Carrier mobility

The carrier mobility was investigated to further evaluate the photocatalytic performance of the heterojunctions. Generally, high carrier mobility could potentially improve the charge utilization for redox reactions before their recombination.[25,52] Two directions of x and y were investigated as shown in Fig. S6.†

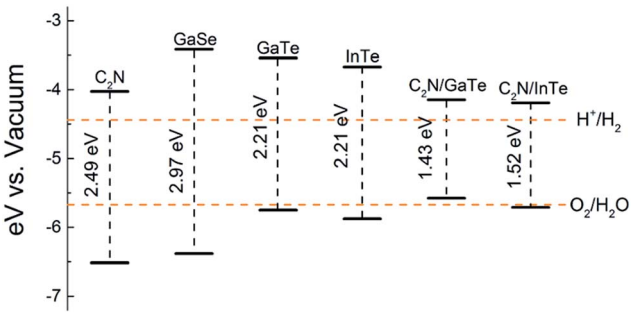

Fig. 3 Band edge positions of isolated monolayers and heterojunctions. The redox potentials of water splitting are represented by orange dashed lines.

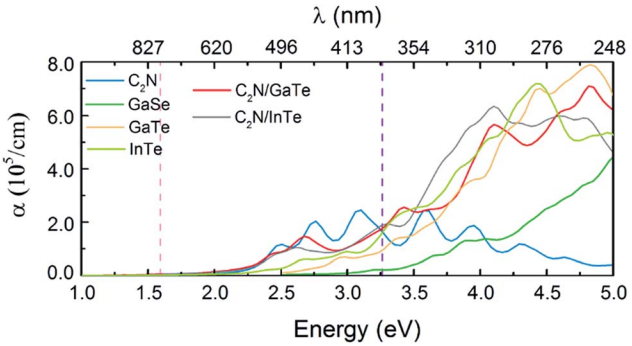

Fig. 4 Optical absorption coefficients for the isolated C_2N, GaSe, GaTe, and InTe monolayers as well as C_2N/GaTe and C_2N/InTe heterojunctions. The area between the red and the purple lines represents the visible-light range.

The effective masses of electrons (m^*_e) and holes (m^*_h) are computed by fitting parabolic functions to the CBM and VBM along the transport direction. The m^*_e and m^*_h along the directions of x and y for the isolated C_2N, GaTe and InTe monolayers as well as C_2N/GaTe and C_2N/InTe heterojunctions are shown in Tables S4† and 1. The m^*_h of the C_2N monolayer is much higher than the m^*_e of C_2N, indicating much lower hole mobility in the C_2N monolayer, consistent with previous reports.[25] For GaTe and InTe, the m^*_h is also larger than m^*_e, which agrees well with previously reported data,[53,54] indicating the credibility of our results.

To calculate the in-plane stiffness and DP constant, the relative energy and band edge positions of the CBM and VBM as a function of the uniaxial strain along the transport directions are shown in Fig. 5 and S7,† respectively. Based on the calculated effective masses, in-plane stiffness and DP constant, the carrier mobility of the isolated monolayers and heterojunctions could be obtained and are shown in Tables S4† and 1. In heterojunctions, the electron and hole mobility can become very high, which could be attributed to the improved in-plane stiffness and more dispersed valence band. The carrier mobility of C_2N/GaTe and C_2N/InTe is higher than that of many 2D semiconductors, such as MoS_2 (ref. 38) and BN monolayers,[55] and comparable to that of MXenes[39] and phosphorene.[56] The improved carrier mobility indicates that the transfer of carriers

Table 1 Effective mass $|m^*|$ (m_e, mass of free electrons), in-plane stiffness C (N m^{-1}), DP constant $|E_1|$ (eV) and carrier mobility μ_{2D} ($cm^2\ V^{-1}\ s^{-1}$) for electrons and holes for C_2N/GaTe and C_2N/InTe heterojunctions along the directions of x and y, respectively

		$\lvert m^*\rvert$	C	$\lvert E_1\rvert$	μ_{2D}
C_2N/GaTe	e_x	0.82	222.11	2.60	685.67
	h_x	1.06	222.11	1.55	1163.21
	e_y	0.38	219.03	2.55	3229.29
	h_y	0.86	219.03	1.82	1251.53
C_2N/InTe	e_x	0.39	207.12	3.35	1744.56
	h_x	0.24	207.12	8.84	613.05
	e_y	0.42	207.04	3.54	1330.34
	h_y	0.31	207.04	8.88	390.98

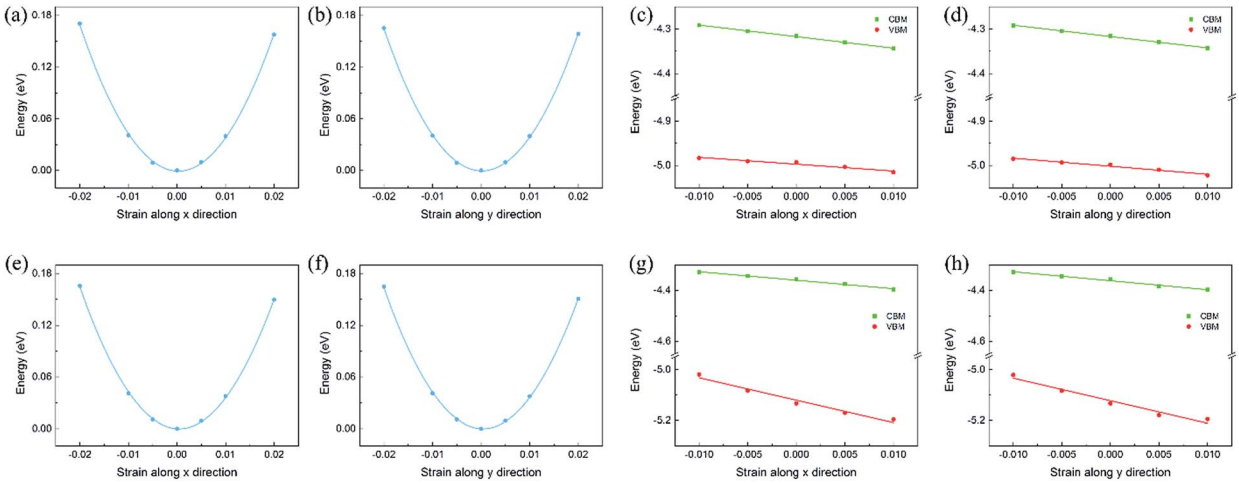

Fig. 5 The relationship between energy and strain for (a, b) C_2N/GaTe and (e, f) C_2N/InTe. The CBM and VBM along the *x* and *y* directions as a function of deformation proportion for (c, d) C_2N/GaTe and (g, h) C_2N/InTe.

to reactive sites is easier during the photocatalytic process. Besides, due to the short distance for the photogenerated electrons and holes to migrate in 2D nanosheets, the recombination of photogenerated carriers is further reduced. Therefore, it can be inferred that the photocatalytic activity of the C_2N/MX heterojunctions would be very good.

To further evaluate the separation of the charge carrier, the exciton binding energies (E_b) were also calculated as shown in Table S5.† The E_b of C_2N was calculated to be 1.24 eV, which is consistent with those in previous reports.[25,57] C_2N/GaTe and C_2N/InTe exhibit much lower E_b values of 0.31 and 0.13 eV, respectively, indicating easier separation of carriers.

HER and OER catalytic activity

The HER and OER catalytic activity is critically important for overall water splitting photocatalysts. The HER performance was evaluated from ΔG_H, which was widely used in previous reports.[58–61] The OER catalytic activity was checked by using the free energy change of each step.[62–65]

Since the CBM of C_2N/GaTe and C_2N/InTe heterojunctions is mainly contributed by C_2N while the VBM mostly comes from the MX, the HER performance of the C_2N layer and the OER catalytic activity of the MX layer were calculated. The ΔG_H with different hydrogen coverages on the C_2N layer is shown in Fig. 6.

The ΔG_H of the first two hydrogen atoms is too negative, indicating that the bonding is too strong. The ΔG_H of the third hydrogen could reach 0.08 and 0.03 eV for C_2N/GaTe and C_2N/InTe, respectively, which are very close to zero, implying that C_2N/GaTe and C_2N/InTe are potentially excellent catalysts for the HER at an appropriate H coverage. The fourth hydrogen atom adsorbed on the C_2N/GaTe and C_2N/InTe heterojunctions would be close to the MX layer (Fig. S8†), leading to a positive ΔG_H.

Then the OER performance of MX in the heterojunctions was investigated. In order to calculate the limiting step of the OER, the free energy of each elementary step (ΔG_1 – ΔG_4) was computed. The free energy diagrams of OER elementary steps on MX layers are shown in Fig. 7.

For both C_2N/GaTe and C_2N/InTe heterojunctions, ΔG of the first three steps is positive while the last step is negative. The third step is the rate-limiting step with a ΔG of 2.70 and 2.17 eV for C_2N/GaTe and C_2N/InTe, respectively. At the standard reduction potential of water oxidation (1.23 eV), the ΔG of the rate-limiting step will decrease to 0.94 eV for C_2N/InTe, which is comparable to and even lower than that of many TM@C catalysts or metal oxides.[66]

The stability of C_2N in water has been experimentally confirmed[24] while the MX has been proven to be stable by calculating their enthalpy of solvation.[26] Therefore, the C_2N/MX heterojunctions would be stable in water. Overall, both C_2N/GaTe and C_2N/InTe are type-II heterojunctions with strong absorption in both visible and near ultraviolet regions and high carrier mobility. Especially, C_2N/InTe is a direct-band-gap heterojunction and exhibits excellent catalytic performance

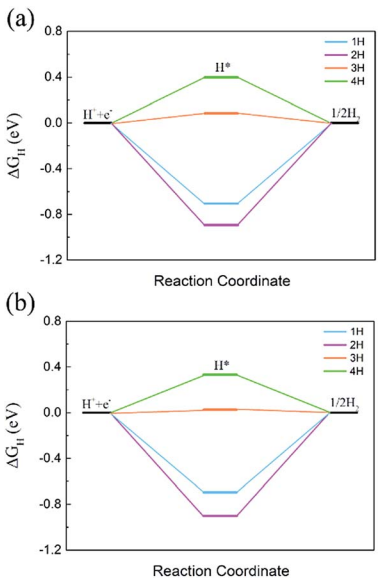

Fig. 6 ΔG_H with different hydrogen coverages on the C_2N layer in (a) C_2N/GaTe and (b) C_2N/InTe heterojunctions.

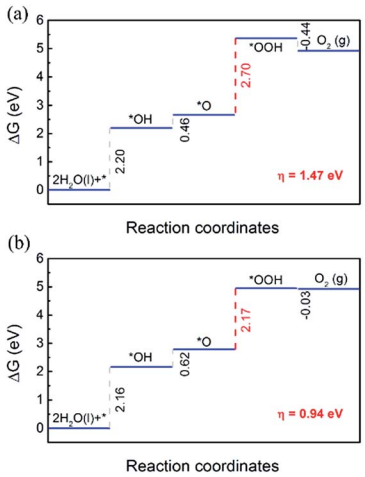

Fig. 7 Free energy diagram for the OER on MX in (a) C_2N/GaTe and (b) C_2N/InTe.

towards both the HER and the OER, indicating that it is a very promising photocatalyst for overall water splitting.

Conclusions

In conclusion, based on band edge positions and lattice parameters, we found that several kinds of MX monolayers can be used to fabricate type-II heterojunctions with C_2N monolayers. By means of first-principles computations, we systematically investigated the photocatalytic performance of C_2N/GaTe and C_2N/InTe heterojunctions for overall water splitting. The results indicate that both are type-II heterojunctions, promoting the efficient spatial separation of electron–hole pairs; therefore, overcoming the electron–hole recombination issue. Interestingly, the C_2N/InTe heterojunction exhibits a direct band gap. The band edge positions from the HSE06 functional predict that their band edges straddle water redox potentials, satisfying the requirements for photocatalytic water splitting. Besides, C_2N/GaTe and C_2N/InTe heterojunctions exhibit strong absorption in both visible and near ultraviolet regions. The calculations of carrier mobility illustrate that the heterojunctions possess higher carrier mobility compared with isolated monolayers, indicating that the transfer of charge carriers to the reactive sites is easier, reducing the probability of recombination of photogenerated carriers. The ΔG_H can reach 0.08 and 0.03 eV for C_2N/GaTe and C_2N/InTe heterojunctions, respectively, leading to a high HER catalytic activity. Moreover, the C_2N/InTe heterojunction possesses a good OER catalytic performance. These results indicate that C_2N/GaTe and C_2N/InTe heterojunctions, especially C_2N/InTe, are very promising photocatalysts for water splitting. Our findings could be helpful to rationally design more type-II heterojunctions for photocatalytic water splitting.

Conflicts of interest

There are no conflicts to declare.

Acknowledgements

This work was supported by the National Natural Science Foundation of China (21421001). The computations were performed on the Magic Cube at the Shanghai Supercomputer Center.

Notes and references

1 X. Chen, S. Shen, L. Guo and S. S. Mao, *Chem. Rev.*, 2010, **110**, 6503–6570.
2 S. Y. Reece, J. A. Hamel, K. Sung, T. D. Jarvi, A. J. Esswein, J. J. H. Pijpers and D. G. Nocera, *Science*, 2011, **334**, 645–648.
3 A. Fujishima and K. Honda, *Nature*, 1972, **238**, 37–38.
4 A. Kudo and Y. Miseki, *Chem. Soc. Rev.*, 2009, **38**, 253–278.
5 Y. Tachibana, L. Vayssieres and J. R. Durrant, *Nat. Photonics*, 2012, **6**, 511–518.
6 J. Yang, D. Wang, H. Han and C. Li, *Acc. Chem. Res.*, 2013, **46**, 1900–1909.
7 M. Z. Rahman, K. Davey and S.-Z. Qiao, *J. Mater. Chem. A*, 2018, **6**, 1305–1322.
8 J. Ran, W. Guo, H. Wang, B. Zhu, J. Yu and S. Z. Qiao, *Adv. Mater.*, 2018, **30**, 1800128.
9 J. Ran, B. Zhu and S. Z. Qiao, *Angew. Chem., Int. Ed.*, 2017, **56**, 10373–10377.
10 J. Ran, G. Gao, F.-T. Li, T.-Y. Ma, A. Du and S.-Z. Qiao, *Nat. Commun.*, 2017, **8**, 13907.
11 A. K. Singh, K. Mathew, H. L. Zhuang and R. G. Hennig, *J. Phys. Chem. Lett.*, 2015, **6**, 1087–1098.
12 X. Zhang, X. Zhao, D. Wu, Y. Jing and Z. Zhou, *Adv. Sci.*, 2016, **3**, 1600062.
13 M. Zhou, X. W. Lou and Y. Xie, *Nano Today*, 2013, **8**, 598–618.
14 D. Wu, X. Zhang, Y. Jing, X. Zhao and Z. Zhou, *Nano Energy*, 2016, **28**, 390–396.
15 X. Zhang, Z. Zhang, D. Wu, X. Zhang, X. Zhao and Z. Zhou, *Small Methods*, 2018, **2**, 1700359.
16 X. Zhang, Z. Zhang, X. Zhao, D. Wu, X. Zhang and Z. Zhou, *J. Mater. Chem. A*, 2017, **5**, 2870–2875.
17 X. Wang, K. Maeda, A. Thomas, K. Takanabe, G. Xin, J. M. Carlsson, K. Domen and M. Antonietti, *Nat. Mater.*, 2009, **8**, 76–80.
18 T. A. Shifa, F. Wang, Z. Cheng, P. He, Y. Liu, C. Jiang, Z. Wang and J. He, *Adv. Funct. Mater.*, 2018, **28**, 1800548.
19 Z. Cheng, T. A. Shifa, F. Wang, Y. Gao, P. He, K. Zhang, C. Jiang, Q. Liu and J. He, *Adv. Mater.*, 2018, 1707433.
20 H. Wang, L. Zhang, Z. Chen, J. Hu, S. Li, Z. Wang, J. Liu and X. Wang, *Chem. Soc. Rev.*, 2014, **43**, 5234–5244.
21 S. J. A. Moniz, S. A. Shevlin, D. J. Martin, Z.-X. Guo and J. Tang, *Energy Environ. Sci.*, 2015, **8**, 731–759.
22 J. Mahmood, E. K. Lee, M. Jung, D. Shin, I. Y. Jeon, S. M. Jung, H. J. Choi, J. M. Seo, S. Y. Bae, S. D. Sohn, N. Park, J. H. Oh, H. J. Shin and J. B. Baek, *Nat. Commun.*, 2015, **6**, 6486.
23 M. R. A. Kishore and P. Ravindran, *ChemPhysChem*, 2017, **18**, 1526–1532.
24 L. Wang, X. Zheng, L. Chen, Y. Xiong and H. Xu, *Angew. Chem., Int. Ed.*, 2018, **57**, 3454–3458.

25 R. Kumar, D. Das and A. K. Singh, *J. Catal.*, 2018, **359**, 143–150.
26 H. L. Zhuang and R. G. Hennig, *Chem. Mater.*, 2013, **25**, 3232–3238.
27 G. Kresse and J. Furthmüller, *Phys. Rev. B: Condens. Matter Mater. Phys.*, 1996, **54**, 11169–11186.
28 G. Kresse and D. Joubert, *Phys. Rev. B: Condens. Matter Mater. Phys.*, 1999, **59**, 1758–1775.
29 J. P. Perdew, K. Burke and M. Ernzerhof, *Phys. Rev. Lett.*, 1996, **77**, 3865–3868.
30 S. Grimme, J. Antony, S. Ehrlich and H. Krieg, *J. Chem. Phys.*, 2010, **132**, 154104.
31 S. Grimme, S. Ehrlich and L. Goerigk, *J. Comput. Chem.*, 2011, **32**, 1456–1465.
32 H. J. Monkhorst and J. D. Pack, *Phys. Rev. B: Solid State*, 1976, **13**, 5188–5192.
33 S. Kümmel and L. Kronik, *Rev. Mod. Phys.*, 2008, **80**, 3–60.
34 J. Heyd, G. E. Scuseria and M. Ernzerhof, *J. Chem. Phys.*, 2003, **118**, 8207–8215.
35 J. Bardeen and W. Shockley, *Phys. Rev.*, 1950, **80**, 72–80.
36 M.-Q. Long, L. Tang, D. Wang, L. Wang and Z. Shuai, *J. Am. Chem. Soc.*, 2009, **131**, 17728–17729.
37 J. Qiao, X. Kong, Z.-X. Hu, F. Yang and W. Ji, *Nat. Commun.*, 2014, **5**, 4475.
38 Y. Cai, G. Zhang and Y.-W. Zhang, *J. Am. Chem. Soc.*, 2014, **136**, 6269–6275.
39 X. Zhang, X. Zhao, D. Wu, Y. Jing and Z. Zhou, *Nanoscale*, 2015, **7**, 16020–16025.
40 Y. Jing, X. Zhang, D. Wu, X. Zhao and Z. Zhou, *J. Phys. Chem. Lett.*, 2015, **6**, 4252–4258.
41 M. Gajdoš, K. Hummer, G. Kresse, J. Furthmüller and F. Bechstedt, *Phys. Rev. B: Condens. Matter Mater. Phys.*, 2006, **73**, 045112.
42 H. H. Wu, Q. Meng, H. Huang, C. T. Liu and X. L. Wang, *Phys. Chem. Chem. Phys.*, 2018, **20**, 3608–3613.
43 S. Saha, T. P. Sinha and A. Mookerjee, *Phys. Rev. B: Condens. Matter Mater. Phys.*, 2000, **62**, 8828–8834.
44 J. K. Nørskov, J. Rossmeisl, A. Logadottir, L. Lindqvist, J. R. Kitchin, T. Bligaard and H. Jónsson, *J. Phys. Chem. B*, 2004, **108**, 17886–17892.
45 Y.-A. Zhu, D. Chen, X.-G. Zhou and W.-K. Yuan, *Catal. Today*, 2009, **148**, 260–267.
46 H. Wang, X. Li and J. Yang, *ChemPhysChem*, 2016, **17**, 2100–2104.
47 T. Björkman, A. Gulans, A. V. Krasheninnikov and R. M. Nieminen, *Phys. Rev. Lett.*, 2012, **108**, 235502.
48 Z. Liu, J. Z. Liu, Y. Cheng, Z. Li, L. Wang and Q. Zheng, *Phys. Rev. B: Condens. Matter Mater. Phys.*, 2012, **85**, 205418.
49 S. Chen, L. Zuzhang, Z. Jian and S. Zhimei, *2D Mater.*, 2017, **4**, 015027.
50 J. Wang, Z. Guan, J. Huang, Q. Li and J. Yang, *J. Mater. Chem. A*, 2014, **2**, 7960–7966.
51 W. Hu, L. Lin, R. Zhang, C. Yang and J. Yang, *J. Am. Chem. Soc.*, 2017, **139**, 15429–15436.
52 T. Luttrell, S. Halpegamage, J. Tao, A. Kramer, E. Sutter and M. Batzill, *Sci. Rep.*, 2014, **4**, 4043.
53 L. Huang, Z. Chen and J. Li, *RSC Adv.*, 2015, **5**, 5788–5794.
54 H. Jin, J. Li, Y. Dai and Y. Wei, *Phys. Chem. Chem. Phys.*, 2017, **19**, 4855–4860.
55 S. Bruzzone and G. Fiori, *Appl. Phys. Lett.*, 2011, **99**, 222108.
56 J. Qiao, X. Kong, Z. X. Hu, F. Yang and W. Ji, *Nat. Commun.*, 2014, **5**, 4475.
57 J. Sun, R. Zhang, X. Li and J. Yang, *Appl. Phys. Lett.*, 2016, **109**, 133108.
58 C. Ling, L. Shi, Y. Ouyang and J. Wang, *Chem. Mater.*, 2016, **28**, 9026–9032.
59 G. Gao, A. P. O'Mullane and A. Du, *ACS Catal.*, 2017, **7**, 494–500.
60 G. Gao, S. Bottle and A. Du, *Catal. Sci. Technol.*, 2018, **8**, 996–1001.
61 X. Zhang, A. Chen, Z. Zhang, M. Jiao and Z. Zhou, *J. Mater. Chem. A*, 2018, **6**, 11446–11452.
62 M. Li, L. Zhang, Q. Xu, J. Niu and Z. Xia, *J. Catal.*, 2014, **314**, 66–72.
63 C. Ling, L. Shi, Y. Ouyang, X. C. Zeng and J. Wang, *Nano Lett.*, 2017, **17**, 5133–5139.
64 G. Gao, E. R. Waclawik and A. Du, *J. Catal.*, 2017, **352**, 579–585.
65 Y.-N. Chen, X. Zhang, H. Cui, X. Zhang, Z. Xie, X.-G. Wang, M. Jiao and Z. Zhou, *Energy Storage Materials*, 2018, **15**, 226–233.
66 X. Cui, P. Ren, D. Deng, J. Deng and X. Bao, *Energy Environ. Sci.*, 2016, **9**, 123–129.